Influence of Boundary Conditions on Downstream Behaviour of Eulerian Lagrangian Simulations of Ammonia Sprays

Daniel Bundred*[1], Felix Leach[1]

[1] Thermal Propulsion Systems Research Group, Department of Engineering Science, University of Oxford, United Kingdom
*Corresponding author: daniel.bundred@eng.ox.ac.uk

Abstract
Shipping accounts for roughly 3% of global emissions, set to rise to 10% by 2050 in a business-as-usual scenario. To reduce maritime emissions, ammonia has been suggested as a carbon independent energy vector. Using ammonia for this purpose will initially require a detailed understanding of its behaviour inside combustion applications. Ammonia has a high saturation pressure, so ammonia sprays are regularly superheated. Under superheated conditions, liquids in contact with rough surfaces exhibit heterogeneous nucleation of a gaseous phase, hence contact between the liquid ammonia and injector wall can lead to vapour generation within the nozzle and a two-phase flow at the nozzle exit. Typically, Volume of Fluid simulations are used to examine behaviour in the near nozzle region, however these are computationally expensive and need to be carefully coupled with later Lagrangian Parcel Tracking (LPT) simulations to model the full spray plume. This study explores the effect of varying boundary conditions in the nozzle on downstream plume characteristics within the LPT simulation framework and compares these results with LPT results in the absence of nozzle geometry. To reproduce nucleation effects, a time-varying inflow boundary condition has been established along the nozzle wall, using a user-defined function to couple the inflow rate to the liquid flow rate. The results show that modifications to the pressure condition in the nozzle wall influence both spray penetration and radial distribution of spray mass, with an increase in spray plume width induced in flash boiling cases.

Keywords: Ammonia, Sprays, Flash Boiling, ECN Spray M, Eulerian-Lagrangian

1 Introduction
In support of the Paris Agreement's objective to restrict global average temperature increases to 1.5℃ above pre-industrial levels, the International Maritime Organisation (IMO) has introduced regulations requiring operators to reduce specific emissions by 40% by 2030 while ensuring that at least 5% of their energy is derived from near-zero greenhouse gas (GHG) emission fuels [1]. The baseline for global maritime transportation emissions was approximately 1.076 billion tonnes of CO_{2e} emissions in 2018, constituting 2.89% of total global emissions [2]. Ammonia has been used extensively as a fertiliser since the early 20th century, such that its global annual production reached 145 million tonnes in 2022, ranking it among the most heavily produced chemicals worldwide [3]. Ammonia has been proposed as a potential energy vector to aid in maritime decarbonisation because it can be synthesised from: electrolysed water, atmospheric nitrogen, and renewable energy. When the hydrogen is produced using renewable energy this is referred to in this instance as "green" ammonia [4, 5, 6]. Compared to hydrogen, ammonia offers advantages including a higher energy density, lower energy requirements for liquefaction, and an established safety framework arising from its long-standing utilisation in agriculture [7]. Despite these benefits, ammonia-based combustion poses several challenges arising from: its low laminar flame speed, high autoignition temperature, higher ignition delay, elevated saturation pressure, and significant enthalpy of vaporisation [8, 9, 10, 11]. Ammonia injection processes deviate substantially from those of conventional fuels. The fuel's high saturation pressure frequently leads to injection under superheated conditions. In many cases, spray evolution is dominated by thermal processes in which flash boiling rapidly consumes available thermal energy, governing both macroscopic (e.g., plume shape and penetration) and microscopic (e.g., droplet size distribution) spray characteristics, and these processes can happen within the nozzle if superheat degree is sufficient [12, 13]. While enhanced evaporation and breakup can be favourable for fuel dispersion [14] care needs to be taken to avoid the fuel impinging on walls, which has detrimental results on subsequent combustion [15, 16].

1.1 Superheated Spray Behaviour

Ammonia remains gaseous at room temperature, reflecting its relatively high saturation pressure compared with other fuels. As a result, it exhibits elevated evaporation rates at temperatures substantially below ambient. At 293 K, ammonia's saturation pressure is 8.6 bar [10]. When decompressed at this temperature to atmospheric pressure, ammonia likely undergoes spontaneous nucleation, both at the site of impurities within the fuel and where the fuel contacts rough surfaces such as the nozzle wall [17], with early work suggesting that this rises with $((T_f - T_s)/T_s)^{4.4}$ [18, 19]. This process is different from cavitation, which occurs when the local pressure in the nozzle drops below the saturation pressure because it is thermally driven and could continue into the chamber if the superheat degree remains sufficient. The flow inside the nozzle is expected to be two phase and complicated by the addition of vapour at the saturation pressure of the liquid fuel, which is substantially greater than the downstream chamber pressure [20].

1.2 Experimental Studies on Ammonia Sprays

Recent investigations have examined ammonia sprays generated by diverse injector types under a range of operating conditions [21, 22, 23, 24, 25, 26, 27]. Zhang *et al*. evaluated a swirl injector, studying equivalence ratios and highlighting the spray's dependence on both injection and ambient pressures. Li *et al*. [24] focused on near-field characteristics, uncovering markedly different behaviours under flare-flashing, transition-flashing, and non-flashing regimes. They reported that the onset of flashing occurs at values of $R_P(= P_a/P_{sat})$ between 1 and 0.5, while flare flashing begins below 0.2. Shen *et al*. [28] explored the effect of varying the ambient pressure on spray characteristics for a six-hole injector. They concluded that spray morphology can be split into three regions by superheat index (R_P): drag dominant ($R_P > 0.53$), evaporation dominant ($0.53 > R_P > 0.23$) and spray collapse ($R_P < 0.23$). Pelé *et al*. [21] and Akram *et al*. [23] also investigated a six-hole injector. Pelé *et al*. compared ammonia with ethanol and gasoline under equivalent conditions, finding ammonia sprays exhibited increased liquid penetration compared with other fuels under matched conditions. Akram *et al*. employed a heater to adjust the fuel temperature and reported that both spray penetration and spray area decreased with rising injection temperature; this effect was more pronounced for ammonia than for gasoline. Thermocouple measurements by Okafor *et al*. [29] and Desclaux *et al*. [30] during ammonia injections indicate minimum temperatures of 200–220 K, underscoring potential challenges for flame stability in subsequent combustion processes. Yang *et al*. [27] used a high pressure single hole diesel injector to examine ammonia sprays and noted a large increase in spray angle as R_P decreased, suggesting internal flashing occurs at lower ambient pressures, with non-flashing sprays taking a conical shape.

1.3 Near Nozzle Spray Behaviour

Volume of Fluid (VoF) simulations are useful for detailed internal nozzle flow investigations of ammonia sprays. Kumar and Van Dam [31, 32] showed that significant evaporation occurs within the nozzle and particularly the counterbore under superheated conditions, leading to the spray behaving as an underexpanded jet, suggesting high pressures persist in the nozzle. However, VoF simulations require 10^4-10^5 core-hours per ms of spray simulation as well as requiring 10-100s GB of RAM to produce a sufficiently resolved mesh [33]. It is therefore currently impractical to apply these directly to full engine simulations and insights from these must be incorporated into LPT simulations for this purpose. Detailed simulation of the nozzle and counterbore volumes is not possible in LPT simulations due to the constraints on grid scale imposed by the size of liquid parcels. However, significant internal flash boiling has been demonstrated for flash boiling ammonia sprays, suggesting that downstream spray behaviour will require modification of the inflow boundary conditions to better capture these effects. This study tests the effect of including the nozzle and counterbore geometry along with realistic nozzle boundary conditions in LPT simulations using a user modified version of the CONVERGE software package. Six simulation setups are compared to examine this, and three sets of experimental conditions are simulated to test the sensitivity to changing conditions.

1.4 Case Setup

This study aims to simulate the cases studied by Desclaux *et al*. [30], who collected data for the ECN Spray M single hole injector at a variety of fuel temperatures and ambient pressures. By varying these two independently, they were able to create cases with a range of R_P values. A single hole injector was chosen to avoid the complexities associated with plume-plume interactions in multi-hole injection events. To match the experimental setup, simulations were a 7 ms injection event. In §3.1 different simulation setups are compared for the same set of experimental conditions ($T_{inj} = 293\ K$, $P_a = 2$ bar, $R_P = 0.23$). In §3.2 three cases are chosen with $R_P = 0.1, 0.23\ \&\ 1.69$ to test the simulation's ability to

predict changes to spray morphology. Conditions for these cases are given in §3.2.

2 Numerical Methods

CONVERGE v3.1.12 Computational Fluid Dynamics Software was used to run the simulations in this study [34]. CONVERGE solves the Navier-Stokes equations using a finite volume method for the gas phase. A density based Pressure Implicit with Splitting of Operators algorithm is used to solve the mass and momentum equations. The liquid ammonia is modelled as a distribution of Lagrangian parcels, each containing N_d droplets. The Reynolds Averaged Navier Stokes (RANS) k-ε model is used to account for turbulence and the Redlich-Kwong equation of state is used to model the gas phase. The domain consists of an orthogonal mesh, with cut cells at the domain boundaries. A base grid scale of 2 mm was employed, and CONVERGE's Adaptive Mesh Refinement (AMR) algorithm was used to refine the mesh in high velocity regions by splitting cells into 8 smaller cells. This was used up to three times, yielding a minimum grid scale of 0.25 mm through AMR. Additionally, the mesh was permanently refined in the near nozzle region, with a three layer thick film of varied cell sizes down to 0.125 mm. The mesh is shown at 0.5 ms ASOI in Figure 1. Parameters used in the simulations are displayed in Table 1.

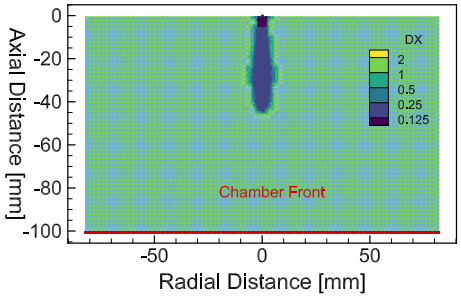

Figure 1. *Slice through $x = 0$ plane showing the full mesh at 0.5 ms ASOI. The Chamber Front (CF) outflow boundary is highlighted.*

Table 1. *Simulation Models Used*

Process	Model
Droplet Introduction	Rate of Injection
Injection	Blob
Equation of State	Redlich-Kwong EoS
Evaporation	Frossling
Turbulence	RANS k-ε STD
Droplet Breakup	KH-RT
Droplet Collision	No Time Counter
Collision Outcomes	Post-Abraham
Droplet Drag	Dynamic

Figure 2 shows a slice through the domain centre. The nozzle ($\varnothing_i = 170$ µm) and counterbore ($\varnothing_o = 400$ µm) are included in the domain, while the sac is not. Lagrangian parcels are added at the nozzle mouth ($[0, 0, -0.1]$) mm, with a diameter of 165 µm. 448,000 parcels are used to model the 7 ms injection event. The rear of the nozzle and the nozzle's curved surface (Nozzle Wall) are used as inflow surfaces for the vapour flow created by the boundary UDF described in §2.2. The bottom of the chamber (at $z = -100$ mm) is used as an outflow boundary. The chamber is 160 mm in diameter and is filled initially with nitrogen at 2 bar and 301 K. Parcels are injected with velocity and diameter determined by the blob injection model, which includes contraction and discharge coefficients. Subsequent primary and secondary breakup is determined by the KH and RT breakup models respectively, and evaporation is modelled using the Frossling correlation. The tuning parameters used are listed in Table 2.

2.1 Rate of Injection

The rate at which liquid mass is added to the simulation domain ($\dot{m}_l(t)$) is a critically important parameter in Lagrangian simulations. The rate profile impacts penetration and the downstream distribution of ammonia liquid and vapour mass. CONVERGE determines the instantaneous rate of injection by scaling the user provided rateshape profile such that the total mass of liquid injected over the course of the simulation is equal to a user provided total over a user specified injection duration. Ideally, experimental results are used to provide the rateshape profile, however, no such data currently exists for the Spray M injector or for any ammonia sprays. The rate profile used is taken from the ECN Spray G injector [35], and the total mass has been reduced to reflect the injector used being single hole. As the Spray G injection event lasts 780 µs (in comparison to the 7 ms injection event studied), it is necessary to modify this profile to avoid reducing the ramp rate at the start/end of injection by stretching the rateshape profile. In order to achieve this, the first 0.3 ms and final 0.2 ms of the rateshape profile were used as the start and end of the modified profile. In between, low amplitude random noise was added to a linear interpolation between these endpoints in order to replicate a representative profile [36]. The modified profile is shown in Figure 3, along with the original Spray G profile.

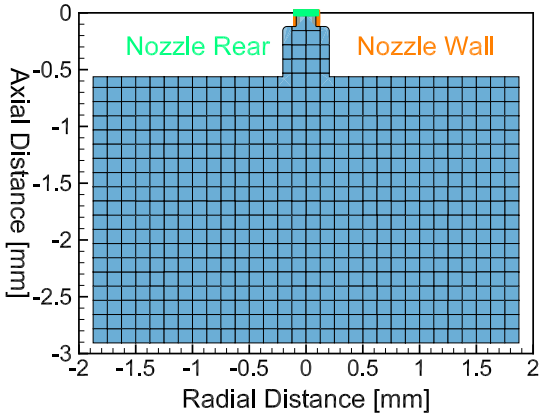

Figure 2. *Slice through $x = 0$ plane showing the mesh in the near nozzle region. The Nozzle Rear (NR) and Nozzle Wall (NW) inflow boundaries are highlighted.*

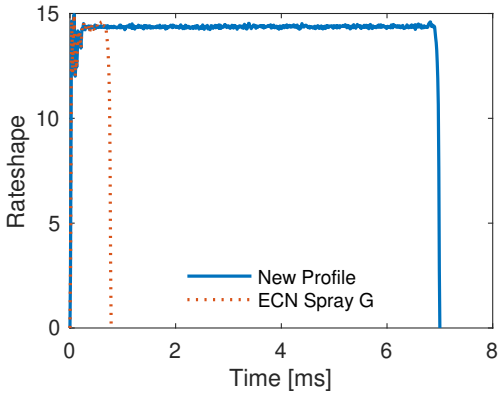

Figure 3. *Rate of injection profile used in this paper, along with the ECN Spray G profile.*

Table 2. *Sub Model Parameters*

Sub Model	Parameter [unit]	Value
Mesh	Base Grid, Min Grid Scale (AMR) [µm]	2000,7.8125
Time Step	Min, Max, Mean [µs]	10^{-4}, 1.9, 9.7×10^{-3}
Lagrangian Initial Conditions	Fuel Temperature [K]	293
Lagrangian Initial Conditions	Droplet Diameter [µm]	165
Lagrangian Initial Conditions	Cone Angle [deg]	5
Kelvin-Helmholtz	Size Constant (B_0)	0.61
Kelvin-Helmholtz	Time Constant (B_1)	5
Rayleigh-Taylor	Size Constant (C_{RT})	0.2
Rayleigh-Taylor	Time Constant (C_1)	0.1

2.2 Boundary Conditions

A User Defined Function (UDF) was written to create a time varying inflow condition at the Nozzle Wall (curved surface of nozzle) and the Nozzle Rear. Contact between the nozzle wall and superheated liquid ammonia could lead to the fuel undergoing heterogeneous nucleation along this surface, and this work relates the resulting vapour pressure to the liquid flow rate. Meanwhile, the injection pressure is much greater than the ambient pressure, so raising the pressure at the Nozzle Rear is necessary to prevent negative pressure induced by flow out of the nozzle. Hence the boundary model reads the liquid flow rate and maps a Dirichlet pressure boundary condition to these boundaries using Eq. 1. Eq. 1 simply maps the mass flow rate onto pressure, so that the pressure varies between P_a when $\dot{m}_l = 0$ and P_{max} when $\dot{m}_l = \dot{m}_{l,max}$. The subscript l refers to the liquid mass flow rate and 0 refers to the unmodified value from the rateshape profile. The mass of vapour entering the domain is then calculated and used to reduce the liquid flow rate through Eq. 2 in order to conserve the total mass of fuel entering the domain. In §3, the effect of varying P_{max} is explored, however typically it either takes P_{inj} or P_{sat}.

$$P_{Boundary} = \begin{cases} P_a + \frac{\dot{m}_{l,0}}{\max(\dot{m}_{l,0})}(P_{max} - P_a) & P_{max} > P_a \\ P_a & P_{max} \leq P_a \end{cases} \tag{1}$$

$$\dot{m}_l = \dot{m}_{l,n-1}\left(1 - \frac{\dot{m}_{v,n-1}}{\dot{m}_{l,n-1}}\right) \quad \text{for} \quad \dot{m}_{v,n-1} < \dot{m}_{l,n-1} \tag{2}$$

The inflowing gas is assumed to be pure ammonia at the same temperature as the liquid fuel. The pressure profile is driven by the user inputted rate of injection profile set pre-simulation. Eq. 2 then

reduces the liquid mass of each of the injected parcels (m_p) by altering the N_d (Eq. 3) parameter, thereby reducing the injected mass without affecting the radius distribution of the droplets at injection, which would both directly and indirectly (through breakup and evaporation) affect the droplet size distribution in the domain. Eq. 2 is limited to avoid setting $N_d < 0$, however as shown in §3.1 $m_v \ll m_l$ for all simulations and so this is not necessary.

$$m_p = \frac{4}{3} N_d \rho_l \pi r_d^3 \tag{3}$$

2.3 Radial Mass Profile Estimation

In order to plot the radial distribution of liquid mass in §3.1 and §3.2, the discrete distribution of parcel values has been translated into a density function. To do this, the spray length has first been split into four bins bounded by the quartiles of the penetration length (L_{99}). L_{99} is based on the 99$^{\text{th}}$ percentile of liquid mass sorted by distance from the injector. This controls for penetration and ensures similar regions of the spray are compared. For each bin, the parcels bounded by that volume are taken and used to estimate a Population Density Function ($\widehat{f_h}$). This is calculated using a Weighted Gaussian Kernel Density Estimate (Eq. 4).

$$\widehat{f_h}(r) = \frac{1}{\sqrt{2\pi} h \sigma \sum_{i=1}^{n_p} m_i} \sum_{i=1}^{n_p} m_i \exp\left(\frac{-(r - r_i)^2}{2h^2\sigma^2} \right) \tag{4}$$

Where n_p is the total number of parcels, m_i is the mass of the i^{th} parcel, r is radial position, r_i is the radial position of the i^{th} parcel and σ is the standard deviation of the parcel distribution. Thus, each parcel contributes a Gaussian Kernel proportional to its mass (Eq. 3) and with standard deviation $h\sigma$ to the PDF, which is then normalised by the total mass ($\sum_i^{n_p} m_i$). The bandwidth (h) is calculated using the Silverman method [37] (Eq. 5) to prevent over or under smoothing of the PDF. IQR refers to the inter quartile range of the parcel distribution.

$$h = 0.9 \min\left(\sigma, \frac{IQR}{1.34} \right) n_p^{-\frac{1}{5}} \tag{5}$$

3 Results and Discussion

3.1 Model Validation

In this section the model's results are examined and compared with a baseline to determine whether its behaviour is as expected. High fidelity modelling of the near nozzle region is best performed using Volume of Fluid (VoF) simulations. However, these simulations are computationally expensive and require tens of thousands of core-hours to run [33]. This model aims to improve the downstream plume characteristics of Lagrangian Parcel Tracking (LPT) simulations by modifying the nozzle boundary conditions for flash boiling sprays. The lower limit of grid scales within LPT simulations is set by the diameter of parcels injected into the domain as beyond this the interaction between the two phases breaks down. This makes LPT simulations unsuitable for resolving behaviour within the nozzle as the region cannot be resolved in sufficient detail. This study tests results generated by injecting the liquid parcels downstream of the nozzle itself (within the counterbore) and examines the effects of this on the spray plume downstream of the nozzle exit on a macroscopic rather than microscopic scale. Six cases are compared for the same set of experimental conditions ($T_{inj} = 293\ K\ P_a = 2$ bar, $T_a = 301\ K$). This case is flashing with a superheat index ($R_P = 0.23$), lying at the edge of the flare flash boiling region [21, 28]. To test the model, six simulations were run for this case they are detailed in Table 3. The default boundary condition type is wall, which makes the boundary behave as a solid surface. The model sets boundaries to inflow boundaries and sets a Dirichlet pressure condition, where this has been used in each simulation the boundary is marked "Inflow" in the table and the pressure is given.

These cases are chosen to isolate the effects of including the nozzle geometry from the boundary model. In case (b) the nozzle geometry is included but the boundary conditions are unchanged. Cases (c)-(f) then explore the effect of setting various pressure condition combinations at the Nozzle Wall and Nozzle Rear boundaries to show their independent/additive effects. In the remainder of this subsection, the effect of these models on spray plume characteristics is examined.

Mass Flow Rates

For the boundary condition model to simulate the phase change of liquid ammonia within the nozzle as intended, it is important that the total mass of ammonia added to the simulation is unchanged. The

Table 3. *Simulations Carried out on the $T_{inj} = 293\ K$, $P_a = 2$ bar, $T_{chamber} = 301\ K$ case.*

Simulation Name	Nozzle Geometry	Nozzle Rear (P)	Nozzle Wall (P)
(a) No Geometry	No	Wall	Wall
(b) Geometry	Yes	Wall	Wall
(c) P_{sat} at NR	Yes	Inflow (P_{sat})	Wall
(d) P_{sat} at NW	Yes	Wall	Inflow (P_{sat})
(e) P_{inj} at NR, P_{inj} at NW	Yes	Inflow (P_{inj})	Inflow (P_{inj})
(f) P_{inj} at NR, P_{sat} at NW	Yes	Inflow (P_{inj})	Inflow (P_{sat})

Table 4. *Cumulative mass flows through various boundaries.*

Simulation Name	Nozzle Wall [mg]	Nozzle Rear [mg]	Liquid [mg]	Total [mg]
(a) No Geometry	0	0	1.81	1.81
(b) Geometry	0	0	1.81	1.81
(c) P_{sat} at NR	0	0.03	1.78	1.81
(d) P_{sat} at NW	0.04	0	1.77	1.81
(e) P_{inj} at NR, P_{inj} at NW	0.06	0.1	1.65	1.81
(f) P_{inj} at NR, P_{sat} at NW	0	0.1	1.71	1.81

cumulative mass flows for the six simulations are shown in Table 4. Figure 4 shows mass flow rates into and out of each simulation. Streams are represented as dashed lines and net flows are displayed as solid lines. Figure 4(a) shows the results for the simulation with no nozzle geometry included. In this case, the total inflow is equal to the liquid injection rate and the outflow is out of the chamber front (100 mm axially downstream of the injector) boundary. Total outflow rises to a peak value of 10^{-3} kg/s in the latter half of the simulation, which reduces the net inflow by the same amount. Figure 4(b) shows the results for the simulation with the nozzle geometry but without the nozzle model activated. It is similar to simulation (a). In Figure 4(c) the model is activated setting the boundary pressure at the nozzle rear to the saturation pressure of ammonia at 293 K (8.6 bar) [10].

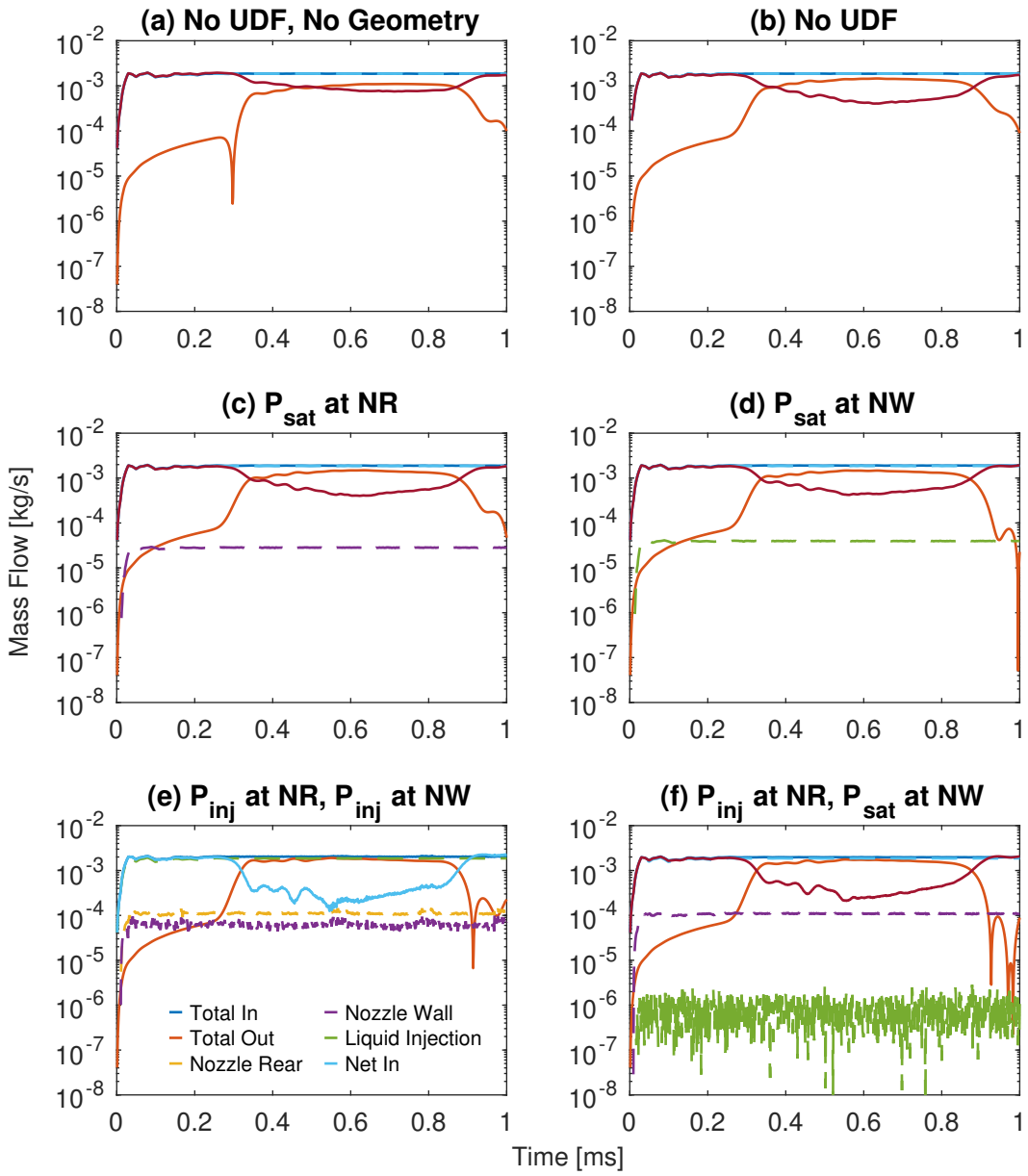

Figure 4. *Mass flow through various boundaries over the simulation time (note the logarithmic scale on the y-axis)*

This creates a second inflow contribution from the vapour flow through the nozzle rear boundary. However, this contribution is two orders of magnitude below the rate of liquid injection and so does not have a noticeable impact on the total or net inflows. Figure 4(d) shows the case where the nozzle wall is set to the saturation pressure of ammonia instead of the nozzle rear. Results for this are similar to simulation (c). The final two simulation cases shown in Figure 4(e)-(f) show the effect of setting the nozzle rear boundary to the injection pressure. In Figure 4(e) the nozzle wall is also set to the injection pressure. This setup is chosen as an edge case to show the extremes of this modelling technique. In reality, there is a pressure drop along the length of the nozzle and hence the pressure at the nozzle wall is significantly lower than the injection pressure. In this case there are contributions to the inflow through both the nozzle rear and nozzle wall boundaries, and their cumulative contribution creates a slight reduction in the liquid mass flow rate through Eq. 2, so a slight deviation between the liquid injection and total inflow lines can be seen. Figure 4(f) shows a case where the nozzle rear pressure was set to the injection pressure but the nozzle wall pressure was set to the saturation pressure (as in (d)). The inflow

through the nozzle wall is thus significantly reduced, however a significant amount of vapour still enters through the nozzle rear and hence there is again a slight deviation between the liquid injection and total inflow lines. Overall, the vapour mass inflow rate is low as a share of the total mass injected, however it is important to note that the density of the injected vapour is multiple orders of magnitude lower than the liquid ammonia, and hence the effect of the vapour is significant beyond its contribution to the mass balance.

Penetration Results and Grid Convergence

A number of parameters influence both the liquid and vapour penetration of Lagrangian simulations. Primarily, the rateshape profile of liquid fuel injected has a large influence on the liquid penetration results. Unfortunately, to the best of the authors' knowledge, no experimental data on the mass of fuel injected is available for ammonia sprays and therefore any tuning of the liquid mass or other parameters which will influence liquid or vapour penetration such as KH or RT model constants does not serve to improve the predictive capability of the simulation. This study therefore does not include any sensitivity analysis relating to these variables. Figures 5-6 show the liquid and vapour penetration results from the six cases shown.

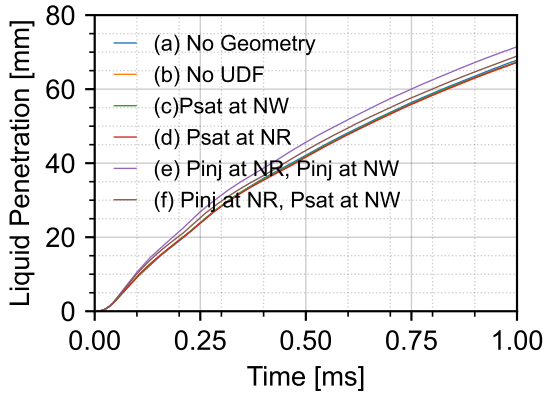

Figure 5. *Liquid penetration length for the six simulations.*

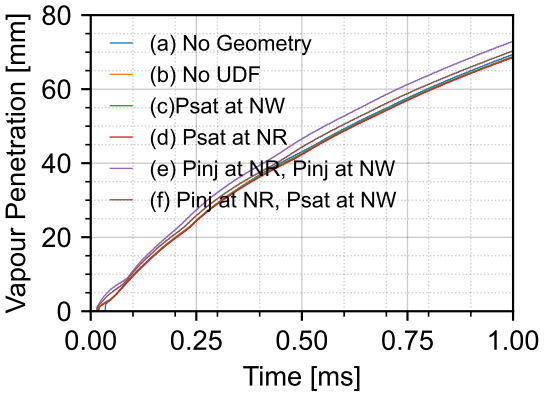

Figure 6. *Vapour penetration length for the six simulations.*

A mesh sensitivity study has been carried out using four different meshes. Each simulation uses the same base grid size of 2 mm. In regions where the velocity in the gas phase exceeds a certain threshold (5 ms^{-1}) the mesh is refined in order to ensure sufficient detail where needed in a computationally efficient way. To test the sensitivity of liquid and vapour penetration to the mesh, the maximum number of times a base grid cell can be refined is varied from 2 to 5, leading to minimum grid scales of 0.5 mm to 0.0625 mm respectively. As the latter is smaller than the radius of injected parcels, it represents a lower limit for the grid scale as beyond this the Lagrangian framework breaks down. From Figures 7-8, it can be seen that although penetration results are not grid independent in this range, they converge around the maximum level of AMR of 4-5. A maximum level of 3 has been used in this study.

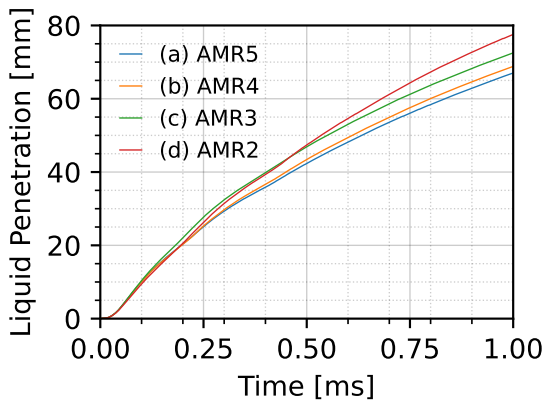

Figure 7. *Liquid penetration length for various levels of grid refinement.*

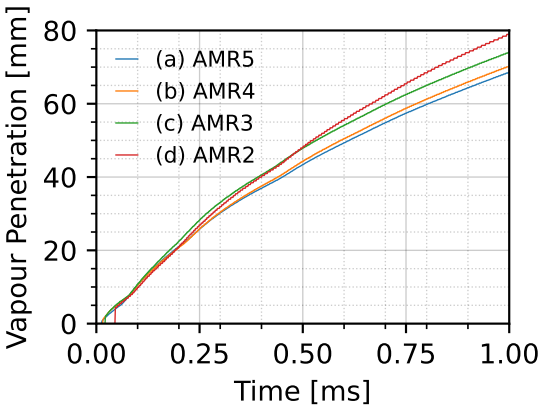

Figure 8. *Vapour penetration length for the various levels of grid refinement.*

Parcel Distributions

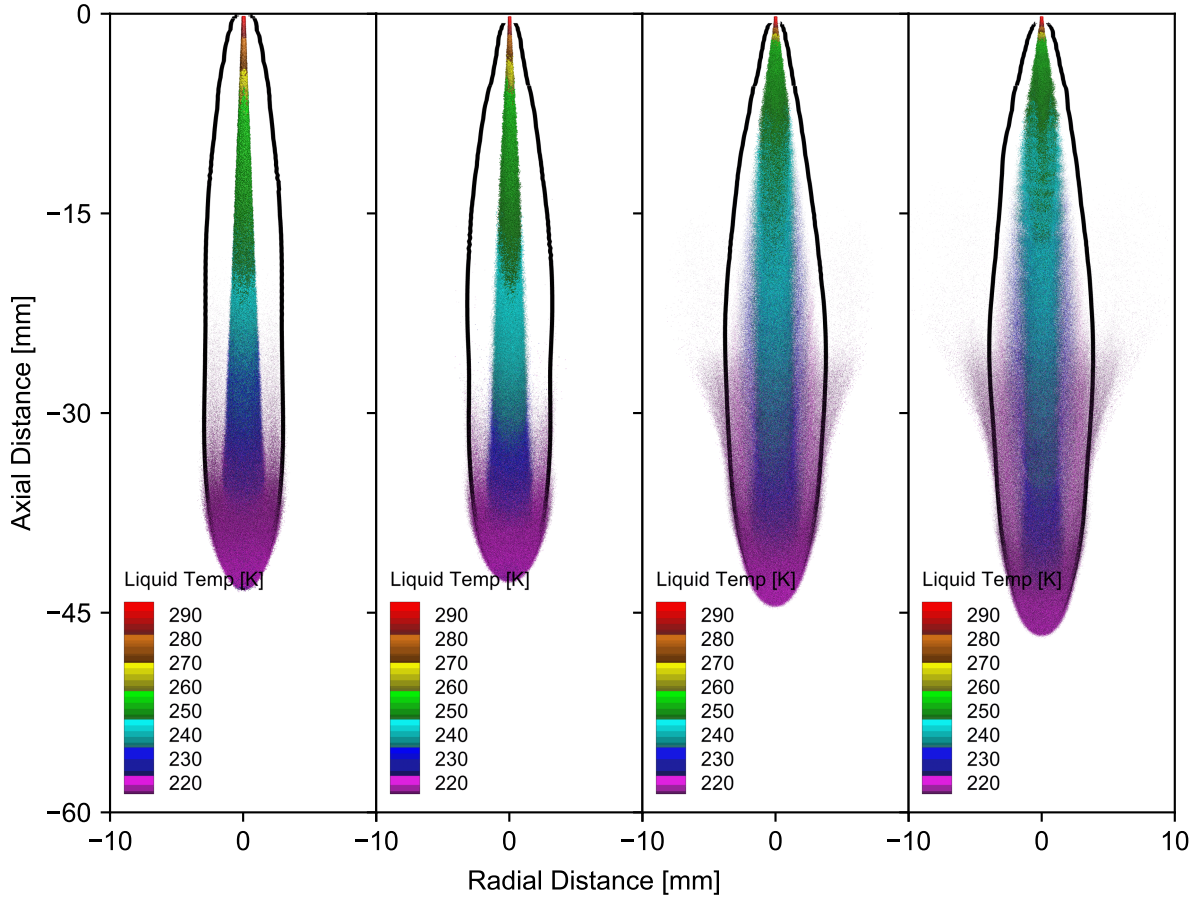

Figure 9. *Spray Images at 0.5 ms ASOI for simulation setups (a - No Geometry), (b - No UDF), (e - P_{inj} at NR, P_{sat} at NW) and (f - P_{inj} at NR, P_{inj} at NW). Parcels are shown as spheres, scaled by their radius and coloured according to their temperature. The black line shows 1% ammonia mass fraction contour for the gas phase*

Changing the pressure boundary conditions in the nozzle has an effect on the downstream velocities of the liquid ammonia parcels. To show this effect, Figure 9 shows a line of sight representation of the field of spray parcels for four of the six simulations ((a),(b),(e) and (f)) at 0.5 ms ASOI. The parcels are scaled by their radius, coloured by their temperature and overlaid on the 1% ammonia mass fraction contour through the $x = 0$ slice, which is shown in black. The spray core is visible in all subplots as a dense conic region originating from the injection point. In Figure 9(a)-(b) the shape of this region is defined by the

cone angle and injection velocity. The cone angle is defined as a parameter a priori, as is the velocity, through the mass flow rate and a combination of the nozzle contraction and discharge coefficients. For all simulations the cone angle parameter is set to 5 degrees in line with the angle observed for non flashing sprays by Desclaux *et al.* [30].

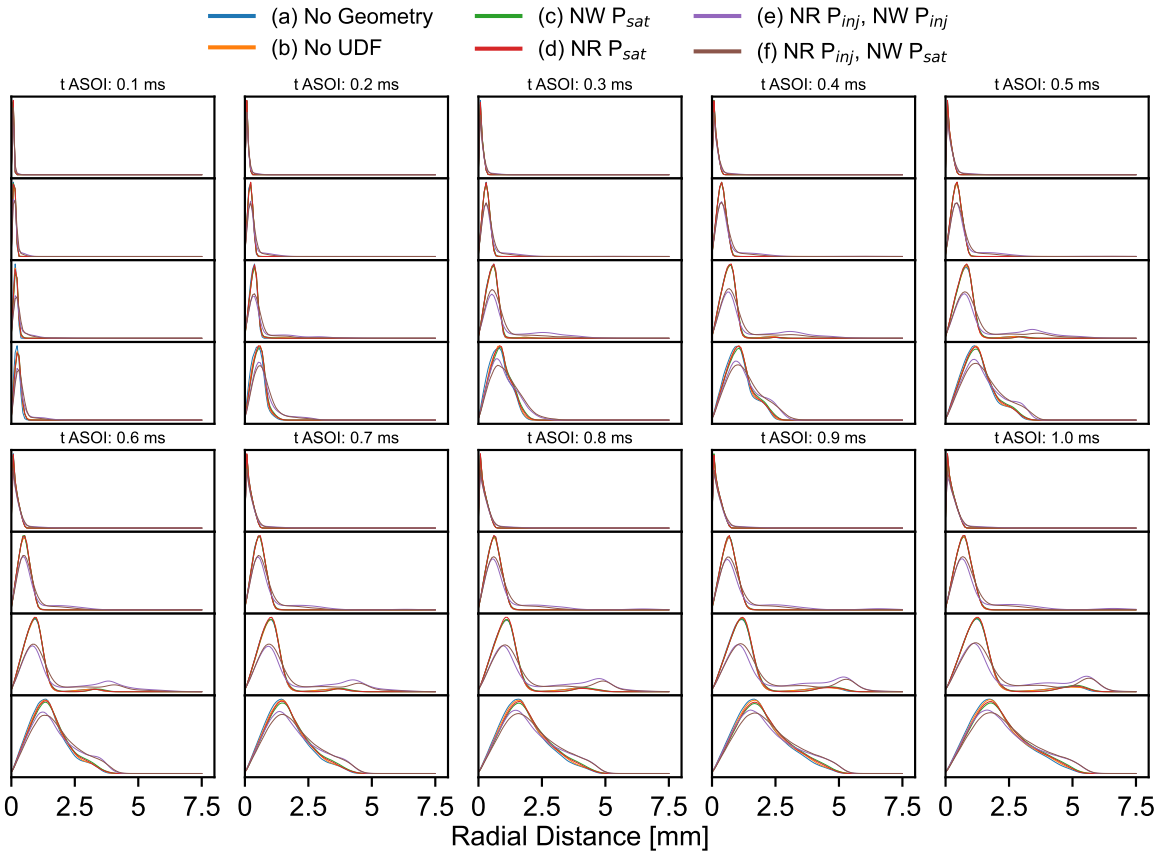

Figure 10. *Time Series of Radial Distribution of Liquid NH_3 Mass*

Figure 9(c)-(d) show the effect of increasing the pressure at the nozzle boundaries. Figure 9(c) shows the cone angle increasing and Figure 9(d) shows the extreme of this, with the cone dispersing nearer to the nozzle into a looser formation of less densely packed parcels. This has the effect of increasing the cone angle of the spray as the expansion of high pressure flow out of the nozzle leads to radial dispersion. Towards the head of the spray, the two cases with the modified boundary conditions (Fig. 9(c)-(d)) have a smaller proportion of their parcels concentrated within the central plume and more within the bulb at the front. The 1% vapour contour line is also shown in black on all images. There is a slight difference in this introduced by adding in the nozzle geometry (Figure 9(a)-(b)) but a larger increase in the width of this line is visible for the simulations with modified boundary conditions (Figure 9(c)-(d)), caused by the increased mean radius of the liquid mass in these cases. In Lagrangian simulations the mass of a liquid parcel is defined by Eq. 3 therefore the mass distribution varies from the distribution of parcel positions once they have been weighted by $N_d R^3$. The radial distribution of liquid mass is shown for all six simulations in Figure 10, which shows the radial distribution of liquid mass, in four axially divided bins at 0.1 ms intervals. The bins are calculated for each simulation by splitting the spray's penetration value at that timestep into four, which is done to ensure that the same section of each spray is compared despite variations in liquid penetration lengths. The limits of each bin are used to isolate a cylindrical volume within which probability density function is estimated for the radial distribution of liquid mass using the mass weighted positions of the parcels and a Gaussian Kernel function as detailed in §2.3. At all times, the top subplot shows the spray core near the nozzle and thus the peak density is at a radius of ≈ 0. Subsequent bins show a peak representing the spray core where the majority of liquid mass is located, followed by a tail representing the density of liquid mass around the spray core. Changes amongst cases (a)-(d) are negligible, however increasing the pressure at the Nozzle Rear to P_{inj} (cases (e)-(f)) leads to a rightward shift in the radial density distribution along the whole length of

the spray but concentrated towards the bulb at the front, which can also be seen in Figure 9. These data show that modifying the pressure boundary conditions in the nozzle has a significant effect on downstream plume shape and the mass distribution of liquid ammonia.

3.2 Sensitivity to Superheat Index

Having established the model's behaviour in §3.1, this section examines the model's sensitivity to the spray cases superheat index. In this section simulation setup f (P_{inj} at NR, P_{sat} at NW) is used to model three experimental cases with varying degrees of superheat. These cases are listed in Table 5. Case (a) represents a non flashing case, while case (c) represents a flare flashing set of conditions where a large increase in plume cone angle is observed experimentally [30] and case (b) lies in between.

Table 5. *Experimental conditions simulated to test model's sensitivity to superheat index.*

Case Name	T_{inj} [K]	P_a [bar]	T_a [K]	R_P
(a) Non-Flashing	263	5	301	1.69
(b) Transition-Flashing	293	2	301	0.23
(c) Flare-Flashing	323	2	301	0.10

Penetration Length

Figs 11 and 12 show the penetration results for the three spray cases. Both the liquid and vapour penetration for non-flashing case are lower as the ambient pressure is much higher (5 bar vs 2 bar). The flare flashing case (c) also shows greater penetration than the transition case, in contradiction with the results of Desclaux *et al*. [30]. The increased pressure in the nozzle region is upstream of the liquid injection point, and thus acts to increase the liquid penetration of the spray. Further work should explore whether this effect can be decoupled from the influence this pressure increase has on the cone angle, as the cone angle needs to increase while spray penetration decreases to match experimental results for different fuel temperatures with the same ambient pressure [30].

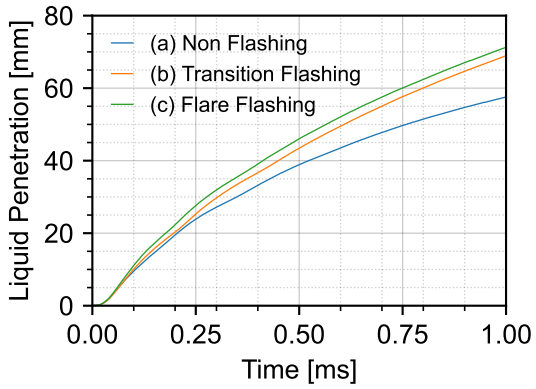

Figure 11. *Liquid penetration length for the three experimental cases.*

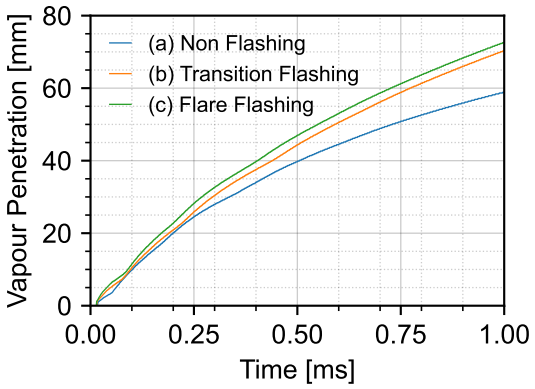

Figure 12. *Vapour penetration length for the three experimental cases.*

Mass Flow Rates

Figure 13 shows the mass flows for the three sets of experimental conditions in the same way as Figure 4 does for the six simulation setups in §3.1. The total inflow is held constant by Eq. 2, meaning that in the non-flashing case (Figure 13(a)) there is a significant reduction in liquid inflow as the inflow through the nozzle rear (the pressure at this boundary is set to P_{inj} reaches a non-negligible fraction of the fuel inflow rate. The inflow through the nozzle wall is seen to increase with the saturation pressure of the fuel increasing. This seems to indicate that the non-flashing case would erroneously display the most extreme response to the modified boundary conditions. However, changing the pressure at the nozzle rear boundary alone does not increase the pressure within the nozzle region and hence does not lead to the same plume expansion observed in the two flashing cases in Figure 14.

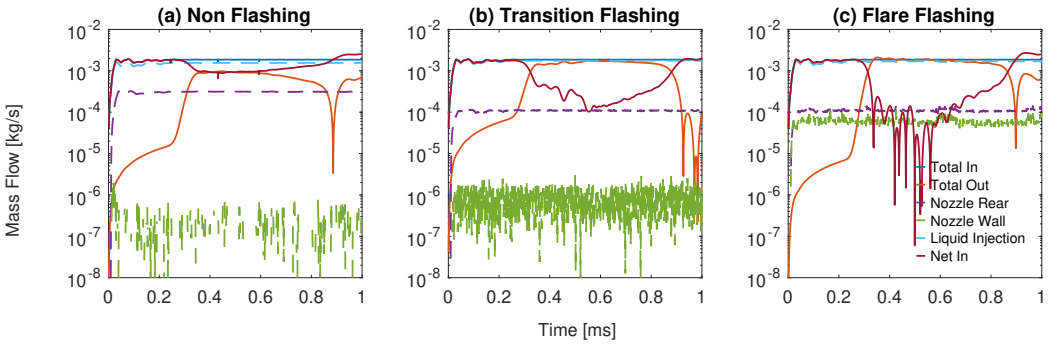

Figure 13. *Mass Flow Through Various Boundaries over the simulation time (note the logarithmic scale on the y-axis)*

In all three of these cases, there is an inversion of the flow through the outflow boundary at around 0.9 ms. This leads to the increase in net inflow seen. In these cases, the return flow is set to be pure nitrogen at the same temperature and pressure as the initial chamber conditions, as this inflow happens significantly downstream of the spray tip (at 100 mm) it does not have a significant influence on the spray plume. The liquid and vapour penetration of (a)<(b)<(c) and therefore the outflow rate increases in line with this, to the extent that it surpasses the rate of inflow at times during the flare flashing simulation (Figure 13(c)). This leads to the net inflow switching from positive to negative and the apparent noise in the signal is caused by the switch between timesteps in this way.

Parcel Distributions

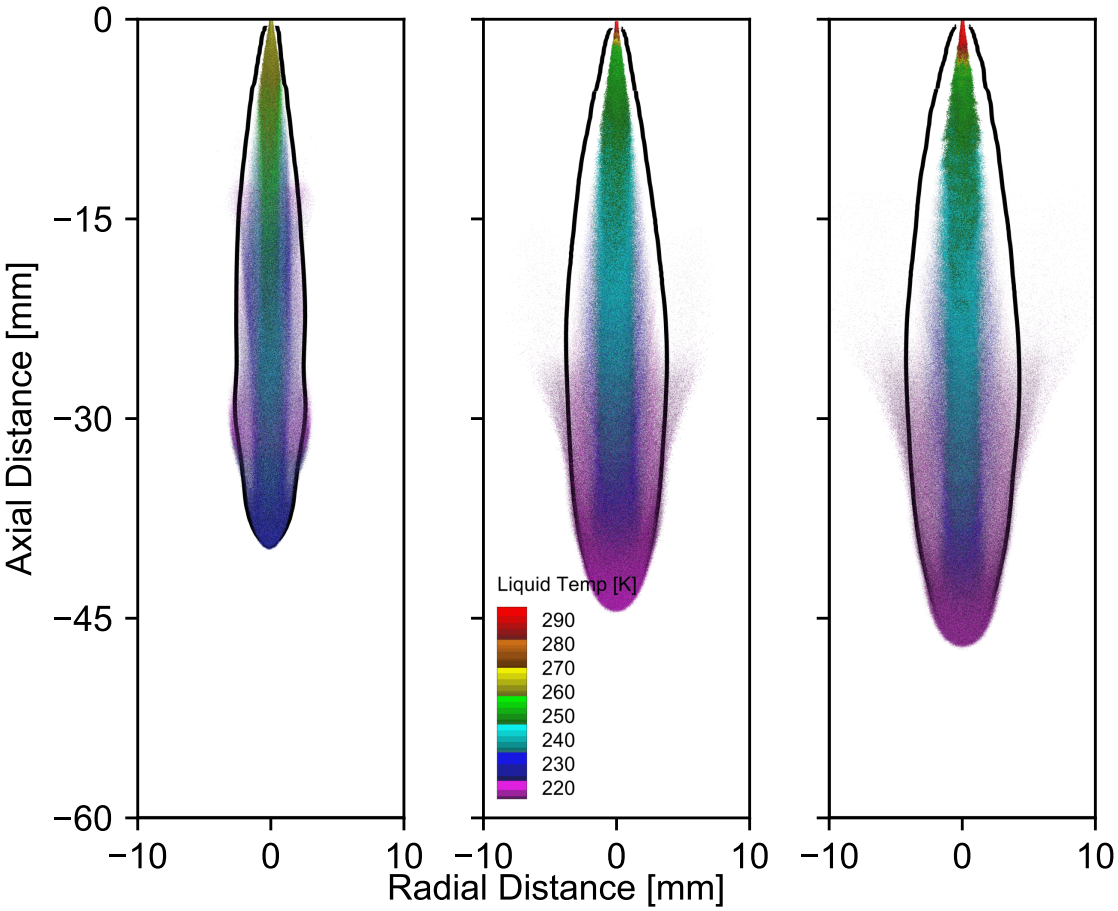

Figure 14. *Spray Images at 0.5 ms ASOI for simulation setups (a) Non Flashing ($P_a = 5$ bar, $R_P = 1.69$), (b) Transition Flashing ($P_a = 2$ bar, $R_P = 0.23$) (c) Flare Flashing $P_a = 2$ bar $R_P = 0.10$). Parcels are shown as spheres, scaled by their radius and coloured according to their temperature. The black line shows the 1% ammonia mass fraction contour for the gas phase*

The plumes at 0.5 ms ASOI are shown for each of the three cases in Figure 14. Again parcels are plotted, sized by their radius and coloured by their temperature, and the 1 % ammonia mass fraction contour is plotted in black for the $x = 0$ plane. Figure 14(b) shows the same results as in Figure 9(c) for the Transition Flashing case. Relative to this, the non-flashing case (Figure 14(a)) shows a narrower contour profile and spray plume, with less substantial cooling and lower penetration. These effects can be attributed to the increased chamber pressure (5 bar vs 2 bar) which reduces liquid penetration and evaporation rates. For the flare flashing case (Figure 14(c)) shows a greater degree of plume expansion, highlighted by the looser packing of parcels in the core of the plume and greater extent of the extremes of the plume. These effects happen despite the ambient pressure being 2 bar in both cases.

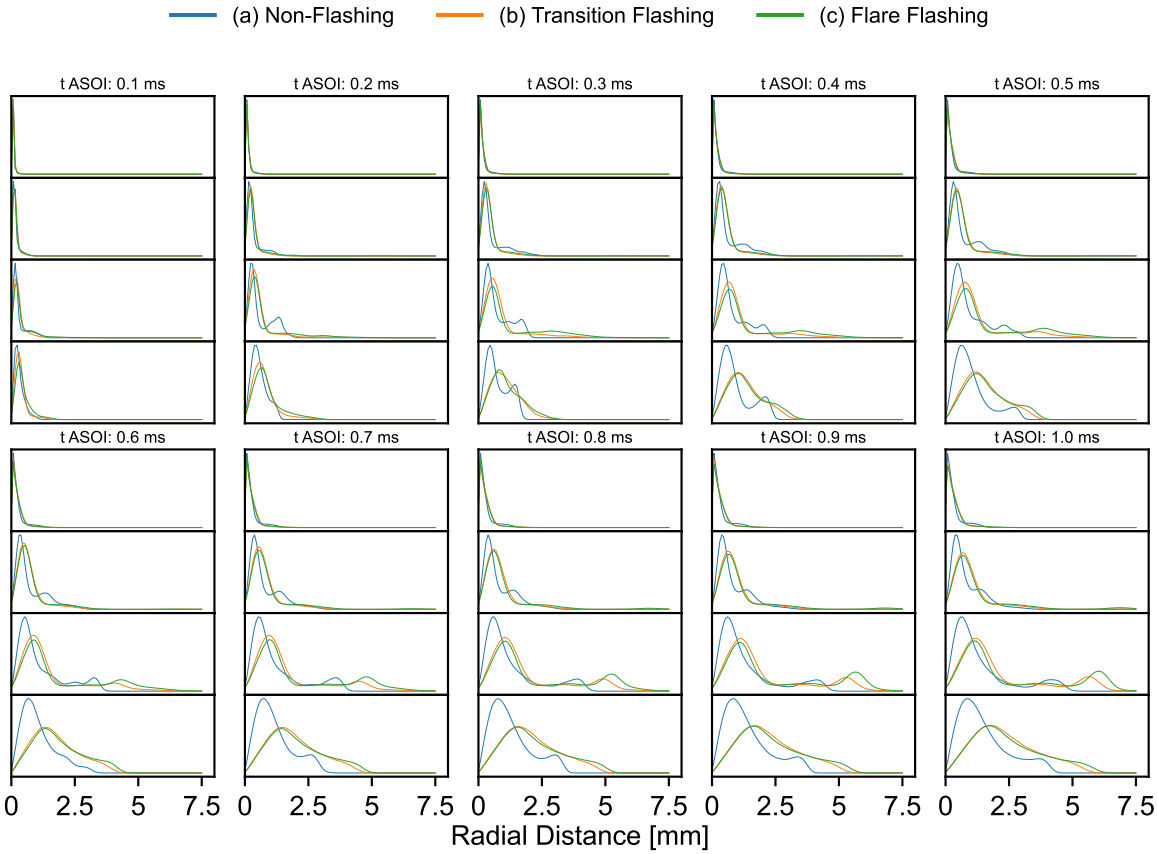

Figure 15. *Time Series of Radial Distribution of Liquid NH_3 Mass for the three experimental cases*

The radial distributions for the three cases are plotted in Figure 15. The same processing technique is used as for Figure 10. The plots show a similar rightwards shift of mass as R_P increases, particularly as the spray develops at later timesteps. The difference between cases (b) and (c) is much less pronounced than the difference caused by increasing the back pressure (a). Despite this, the differences between cases (b) and (c) demonstrate the effect of increasing the pressure at the nozzle wall boundary, as this has increased from 8.6 bar in (b) to 20 bar in (c). It can be seen that the increase leads to further radial spreading of the liquid mass despite the ambient pressure remaining constant.

Conclusions

The effect of incorporating the nozzle and counterbore geometry into LPT simulations has been assessed, and the influence of modifying Dirichlet pressure conditions inside the nozzle geometry has been explored using a variety of boundary condition combinations proportional to the rate of injection profile. A selected simulation framework has then been tested against three different experimental cases with varying degrees of superheat and ambient pressures. Key findings were:

- The nozzle geometry itself has limited effect on spray penetration, spray plume shape or radial mass distribution in LPT simulations.

- Combining the nozzle geometry with increased pressure boundary conditions in the nozzle can have significant impact on liquid penetration, plume shape and the radial mass distribution. The cone angle increases significantly when the pressure at both nozzle boundaries is increased in line with experimental data on flashing ammonia sprays.
- By varying the nozzle wall pressure, up to the saturation pressure of the fuel, it was possible to introduce a degree of sensitivity of the plume's radial distribution to the superheat degree. However, this is accompanied with an increase in penetration due to the increase in axial momentum exchange to the spray parcels.
- Further work is needed to develop a more sophisticated set of boundary conditions in the nozzle, and to explore whether the radial distribution of the liquid mass can be influenced independently of the liquid penetration. The energy consumed in vaporising ammonia within the nozzle should also be considered and removed from the spray by reducing the temperature of the remaining liquid.

Acknowledgements

This research was funded in whole or in part by the Engineering & Physical Sciences Research Council (EPSRC, EP/V04673X/1 & EP/W524311/1). For the purpose of Open Access, the authors have applied a CC BY public copyright license to any Author Accepted Manuscript (AAM) version arising from this submission. Data supporting this paper is available from the "Oxford Research Archive" repository, accessible at `https://ora.ox.ac.uk`.

References

[1] International Maritime Organisation, "2023 strategy on reduction of GHG emissions from ships," (2023).

[2] International Maritime Organisation, "Fourth greenhouse gas study 2020," (2020).

[3] US Geological Survey, "Mineral commodity summaries 2024," (2024).

[4] N. Bora, A. K. Singh, P. Pal, U. K. Sahoo, D. Seth, D. Rathore, S. Bhadra, S. Sevda, V. Venkatramanan, S. Prasad *et al.*, "Green ammonia production: Process technologies and challenges," Fuel **369**, 131808 (2024).

[5] G. Chehade and I. Dincer, "Progress in green ammonia production as potential carbon-free fuel," Fuel **299**, 120845 (2021).

[6] N. Salmon and R. Bañares-Alcántara, "Green ammonia as a spatial energy vector: a review," Sustainable Energy & Fuels **5**, 2814–2839 (2021).

[7] A. Valera-Medina, H. Xiao, M. Owen-Jones, W. I. David, and P. J. Bowen, "Ammonia for power," Progress in Energy and Combustion Science **69**, 63–102 (2018).

[8] J. Li, S. Lai, D. Chen, R. Wu, N. Kobayashi, L. Deng, and H. Huang, "A review on combustion characteristics of ammonia as a carbon-free fuel," Frontiers in Energy Research **9**, 760356 (2021).

[9] A. M. Elbaz, S. Wang, T. F. Guiberti, and W. L. Roberts, "Review on the recent advances on ammonia combustion from the fundamentals to the applications," Fuel Communications **10**, 100053 (2022).

[10] D. R. Stull, "Vapor pressure of pure substances. organic and inorganic compounds," Industrial & Engineering Chemistry **39**, 517–550 (1947).

[11] M. Zander and W. Thomas, "Some thermodynamic properties of liquid ammonia: PVT data, vapor pressure, and critical temperature," Journal of Chemical and Engineering Data **24**, 1–2 (1979).

[12] R. D. Oza and J. F. Sinnamon, "An experimental and analytical study of flash-boiling fuel injection," SAE transactions pp. 948–962 (1983).

[13] Y. Liao and D. Lucas, "Computational modelling of flash boiling flows: A literature survey," International Journal of Heat and Mass Transfer **111**, 246–265 (2017).

[14] W. Zeng, M. Xu, G. Zhang, Y. Zhang, and D. J. Cleary, "Atomization and vaporization for flash-boiling multi-hole sprays with alcohol fuels," Fuel **95**, 287–297 (2012).

[15] M. T. Lewandowski, M. Pasternak, M. Haugsvær, and T. Løvås, "Simulations of ammonia spray evaporation, cooling, mixture formation and combustion in a direct injection compression ignition engine," International Journal of Hydrogen Energy **52**, 916–935 (2024).

[16] S. T. Chin and C.-F. F. Lee, "Numerical investigation of the effect of wall wetting on hydrocarbon emissions in engines," Proceedings of the Combustion Institute **29**, 767–773 (2002).

[17] L. Angelilli, P. P. Ciottoli, R. Malpica Galassi, M. Valorani, F. E. Hernandez-Perez, and H. G. Im, "A thermal flash-boiling model for secondary atomization of lagrangian droplets," in *AIAA SCITECH 2024 Forum,* (2024), p. 1637.

[18] G. Kocamustafaogullari and M. Ishii, "Interfacial area and nucleation site density in boiling systems," International Journal of Heat and Mass Transfer **26**, 1377–1387 (1983).

[19] J. R. Riznic and M. Ishii, "Bubble number density and vapor generation in flashing flow," International Journal of Heat and Mass Transfer **32**, 1821–1833 (1989).

[20] O. Avni, T. Bar-Kohany, and E. Sher, "Flash boiling atomization triggered and driven by intensive radiation," Thermal Science and Engineering Progress **32**, 101334 (2022).

[21] R. Pelé, C. Mounaïm-Rousselle, P. Bréquigny, C. Hespel, and J. Bellettre, "First study on ammonia spray characteristics with a current GDI engine injector," Fuels **2**, 253–271 (2021).

[22] Q. Cheng, K. Ojanen, Y. Diao, O. Kaario, and M. Larmi, "Dynamics of the ammonia spray using high-speed Schlieren imaging," in *SAE Technical Papers,* (SAE International, 2022).

[23] Akram, Muhammad Saad, Yeganeh, Maryam, Cheng, Qiang, Kaario, Ossi, and Larmi, Martti, "Experimental study on flash boiling of ammonia fuel sprays – a potential alternative fuel," in *WCX SAE World Congress Experience,* (SAE International, 2023).

[24] S. Li, T. Li, N. Wang, X. Zhou, P. Yi, and R. Chen, "Effect of near-field characteristics on the two-phase distribution of superheated ammonia spray," International Journal of Engine Research (2023).

[25] Z. Zhang, T. Li, R. Chen, N. Wang, Y. Wei, and D. Wu, "Injection characteristics and fuel-air mixing process of ammonia jets in a constant volume vessel," Fuel **304** (2021).

[26] L. Shen and F. Leach, "Effect of ambient pressure on ammonia sprays using a single hole injector," SAE International Journal of Advances and Current Practices in Mobility **7**, 583–598 (2025).

[27] R. Yang, Q. Tang, H. Cheng, S. Zhang, Y. Zhang, and M. Yao, "Experimental study on the spray characteristics of high-pressure liquid ammonia under different ambient conditions," Journal of the Energy Institute **117**, 101771 (2024).

[28] L. Shen and F. Leach, "An experimental study on the macroscopic behaviours of ammonia sprays in a constant volume chamber," International Journal of Hydrogen Energy **126**, 386–395 (2025).

[29] E. C. Okafor, H. Yamashita, A. Hayakawa, K. D. A. Somarathne, T. Kudo, T. Tsujimura, M. Uchida, S. Ito, and H. Kobayashi, "Flame stability and emissions characteristics of liquid ammonia spray co-fired with methane in a single stage swirl combustor," Fuel **287**, 119433 (2021).

[30] A. Desclaux, R. Pelé, C. Hespel, and C. Mounaïm-Rousselle, "Liquid ammonia injection on single hole injector: effect of initial conditions on flash boiling process," (2023).

[31] A. Kumar and N. V. Dam, "Liquid ammonia sprays for engine applications," Atomization & Sprays (2024).

[32] A. Kumar and N. V. Dam, "Internal nozzle simulations of flash boiling liquid ammonia sprays for engine applications," Atomization and Sprays (2025).

[33] Z. Yue, M. Battistoni, and S. Som, "Spray characterization for engine combustion network spray g injector using high-fidelity simulation with detailed injector geometry," International Journal of Engine Research **21**, 226–238 (2020).

[34] P. Richards and K. Senecal, "CONVERGE CFD manual series CONVERGE manual," (2021).

[35] ECN, "Spray G Operating Condition," https://ecn.sandia.gov/gasoline-spray-combustion/target-condition/spray-g-operating-condition/.

[36] F. Leach, M. H. Davy, M. P. Henry, M. Tombs, and F. Zhou, "A new method for measuring fuel flow in an individual injection in real time," SAE International Journal of Engines **11**, 687–696 (2018).

[37] B. W. Silverman, *Density estimation for statistics and data analysis* (Routledge, 2018).